Remarkable durability of Pt–Ir alloy catalysts supported on graphitic carbon nanocages
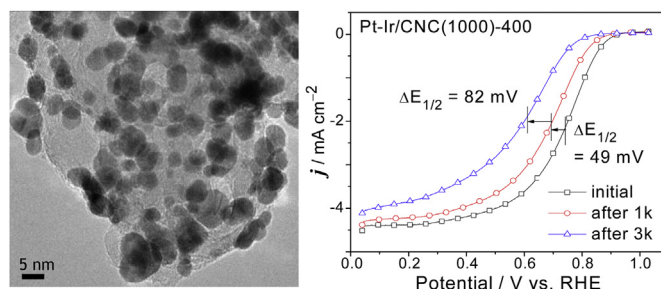
CrossMark

Min Zeng, Xiao Xia Wang, Zhe Hua Tan, Xin Xin Huang, Jian Nong Wang*

Nano-X Research Center, School of Mechanical and Power Engineering, East China University of Science and Technology, 130 Meilong Road, Shanghai 200237, PR China

HIGHLIGHTS

- 3–5 nm Pt–Ir alloy particles were uniformly deposited on carbon nanocages.
- Heat treatment was carried out to improve the degree of alloying.
- Pt–Ir alloy catalyst showed enhanced catalytic performance than pure Pt catalyst.

GRAPHICAL ABSTRACT

ABSTRACT

Low durability is the major challenge hindering the large-scale implementation of proton exchange membrane fuel cell (PEMFC) technology. To improve the electrochemical activity and durability of conventional Pt catalyst used in PEMFCs, we prepare Pt–Ir alloy catalysts supported on homemade graphitic carbon nanocages (CNCs). Results from cyclic voltammetry (CV) and linear sweep voltammetry (LSV) show that the alloy catalyst with an atomic Pt/Ir ratio of 1:1 supported on CNCs with a high degree of graphitization exhibits an excellent electrocatalytic activity. Furthermore, this alloy catalyst shows a drastic improvement in durability and stability over the unalloyed Pt catalyst supported on the same CNCs and the catalyst from a commercial source (Johnson Matthey Co.). It is found that the concurrent uses of well-graphitized CNCs as the support material and Ir as the alloying element are critical for the observed improvement. Such a Pt–Ir alloy catalyst provides a new replacement for the conventional Pt catalyst with not only a drastic improvement in durability but also a reduction in Pt usage by 50% as well.

© 2014 Elsevier B.V. All rights reserved.

1. Introduction

Proton exchange membrane fuel cells (PEMFCs) that convert the chemical energy of hydrogen and oxygen into electrical energy are considered as a promising clean power source for transportation, mobile and stationary applications and have been attracting much attention in recent years. Catalyst is one of the critical components determining the performance, durability and cost and thus the final commercialization of PEMFCs [1]. Within the last decades, much progress had been made for different kinds of anode and cathode catalysts. Up to now, most catalysts being in use are still Pt based in the form of nanoparticles dispersed on carbon black due to the high catalytic activity of Pt. In addition to the high cost of this scarce precious metal, current Pt catalysts also suffer from performance degradation during the practical operations under the conditions of the high voltage and the acidic and oxidative environment in

PEMFCs [2]. The proposed degradation mechanisms mainly include coarsening of Pt particles [3], Pt dissolution [4], Pt poisoning [5], and carbon support corrosion [6]. As a result of these degradation processes, in the PEMFC vehicles in the test fleets monitored by the United States Department of Energy, the stability of the catalyst, together with the whole lot of the membrane electrode assembly, is still short of the 5000-h durability target [1]. Therefore, how to improve the performance and durability with a reduced Pt loading is the subject of the most research activities on electrocatalyst.

In order to reduce the Pt loading, great efforts have been devoted to explore binary and ternary Pt alloys [7], core−shell structures [8] and even non-Pt catalysts [9]. Alloying has been reported to be a promising approach for reducing the Pt loading without losing the activity and durability. Some factors such as alloying element, morphology, and post-treatment have been found to affect the activity and durability of alloy catalysts [10]. Many base metal elements with different ratios, such as Co [11,12], Cu [12], Ni [13], V [14], Fe [15−17], Pd [18], Cr [19], Mn [20], and Au [21], have been studied for alloying with Pt. However, the drawback of these alloy catalysts is the fast dissolution of the non-precious metals into the electrode assembly. The degree of dissolution depends upon the particular base metal used and its atomic ratio with respect to Pt.

Iridium is one of the most stable transition metals in acidic media and much less expensive than Pt [22]. Ir and IrO_x have been proposed as good promoters for Pt/C catalysts also because of their high activity for oxygen revolution, CO and hydrogen oxidation and strong affinity for OH or O species [23,24]. However, alloying Pt with Ir was little studied. Limited data showed that $Ir_xPt_{1−x}$ alloy nanoparticles prepared by a thermolytic reduction method were found to exhibit a good catalytic activity and tolerance to CO poisoning in comparison with Pt nanoparticles [25]. So far, no studies have focused on Pt−Ir alloy catalysts supported on practically useful carbon materials and their stability in accelerated durability test. As a matter of fact, it is still a big challenge to design Pt−Ir alloy catalysts to have a higher activity and durability than conventional Pt catalysts.

In the present study, we report a highly active and durable alloy catalyst: Pt−Ir alloy nanoparticles supported on a homemade carbon material (carbon nanocages-CNCs). The Pt−Ir/CNC catalyst with a nominal metal weight loading of 45% was prepared by the ethylene glycol (EG) reduction of Pt and Ir precursors and then heat treatment. As will be shown, Pt−Ir nanoparticles dispersed uniformly with a size of 3−6 nm on the surface of the CNC support, and the Pt−Ir/CNC catalyst showed a much better activity and durability than the unalloyed Pt catalyst supported on the same CNCs and the commercial Pt/C catalyst from Johnson Matthey Co. (JM).

2. Experimental section

2.1. Synthesis of CNCs

The support used in this study was homemade CNCs with a hollow interior and a graphitic shell. This material was prepared by pyrolysis of the mixture of iron pentacarbonyl ($Fe(CO)_5$) and pyridine (C_5H_5N) with a volume ratio of 1:1 at 700 or 1000 °C. This was followed by heat treatment of the raw material in the presence of NH_4Cl for the purpose of removing iron particles. The CNC supports prepared at 700 and 1000 °C are designated as CNC(700) and CNC(1000), respectively.

2.2. Catalyst preparation

The Pt−Ir/CNC catalyst was prepared by an EG reduction method. Typically, the carbon support was sonicated in EG first.

Then, certain amounts of iridium chloride hydrate ($IrCl_3 \cdot 3H_2O$) and chloroplatinic acid ($H_2PtCl_6 \cdot 6H_2O$) solutions were added into the carbon slurry and stirred for 20 min. The mixture was heated up to 130 °C and refluxed for 3 h under continual vigorous stirring. After having been cooled down to room temperature, the catalyst was filtered and washed with deionized water several times until no $Cl^−$ could be detected by $AgNO_3$ solution. The nominal Pt:Ir atomic ratios were designed to be 3:1, 1:1, and 1:3, and the corresponding alloy catalysts are designated as $Pt_3−Ir_1$, $Pt−Ir$, and $Pt_1−Ir_3$, respectively. The total metal loading (including both Pt and Ir) on the carbon support was controlled to be 45 wt.%.

To optimize the electrocatalytic activity, the as prepared Pt−Ir/CNC(700) sample was further heat-treated at 200, 300 and 400 °C in a tube furnace under vacuum, and the resultant catalysts are referred to as Pt−Ir/CNC(700)-200, Pt−Ir/CNC(700)-300, and Pt−Ir/CNC(700)-400, respectively. For comparison, the Pt−Ir alloy catalysts supported on CNC(1000) and Pt catalysts alloyed with Pd were also synthesized and then heat treated by the same method.

2.3. Physical characterization

Transmission electron microscopy (TEM, JEOL-2100) was applied to investigate the morphology and metal particle dispersion of the samples. The chemical composition analyses were performed using inductively coupled plasma-atomic emission spectroscopy (ICP-AES, iCAP 6000 Radial, THERMO). X-ray diffraction (XRD) analysis was carried out to study the crystallization of as-prepared catalysts. The X-ray diffractometer was operated at 35 kV and 200 mA with nickel-filtered Cu Kα radiation as an incident beam (D/max 2550VL/PC). The chemical elements on the surfaces of the catalysts were analyzed by X-ray photoelectron spectroscopy (XPS, Kratos Axis Ultra DLD X-ray photoelectron spectroscopy). This system used a focused monochromated Al Kα (15 kV) X-ray source for excitation and a spherical section analyzer at a base pressure of $10^{−9}$ Torr. The peak energies were calibrated by placing the major C1s peak at 284.6 eV.

2.4. Electrochemical testing

Cyclic Voltammetry (CV) technique was applied to evaluate the electrochemical activities of all catalysts. The experiments were conducted using a CHI618D instrument in a conventional three electrode cell at a constant temperature. This temperature was controlled to be within 25 ± 2 °C in a water bath in order to minimize the effect of ambient temperature variation between winter and summer or day and night time. The reference and counter electrodes were a saturated calomel electrode (SCE) and a large-area Pt plate, respectively.

The working electrode was prepared as follows: 17.5 mg catalyst was dispersed in a mixture of 4.65 ml ethanol and 0.35 ml 5 wt.% Nafion solution. The mixture was agitated by ultrasonication for 30 min to form an ink. 10 μL of this ink was then dropped on a glassy carbon electrode with a diameter of 3 mm and dried to yield a thin-film electrode. The metal loading on the electrode was 0.2 mg cm$^{−2}$. The electrolyte was 0.5 M H_2SO_4. During the accelerated durability test, cyclic voltammetry was recorded at each set of 500 cycles of potential sweep from 0 to 1.2 V (vs. RHE) at a rate of 100 mV s$^{−1}$, and the potential cycling was up to 3000 cycles in total.

The catalytic activity and durability for oxygen reduction reaction (ORR) were evaluated using a rotating disk electrode (RDE) (Pine, AFMSRCE 3005) by linear sweep voltammetry (LSV). The working electrode was prepared as follows: 4 mg catalyst was dispersed in a 2 ml mixture of methanol and Nafion (5 wt.%) with the mass ratio of 50:1. The mixture was agitated by ultrasonication

for 30 min to form an ink. 10 μL of this ink was then dropped on a glassy carbon electrode with a diameter of 5.6 mm and dried to yield a thin-film electrode. The total metal loading on the RDE was controlled to be 32.48 μg cm^{-2}. Polarization curves were obtained in an O_2-saturated 0.5 M H_2SO_4 solution at 25 °C with a scan rate of 5 mV s^{-1} and rotation rates of 400, 625, 900, 1225, 1600 and 2000 rpm. For the durability study, the RDE was subjected to a potential cycling test. Specifically, the electrode was scanned from 0.6 to 1.2 V (vs. RHE) at a rate of 100 mV s^{-1}. CV and ORR curves were recorded at each set of 1000 cycles. For comparison, a commercial Pt/C catalyst with 40% Pt loading from JM was tested under the same conditions.

3. Results and discussion

3.1. Physical characterization

The TEM images for the CNC support materials prepared at 700 and 1000 °C (CNC(700) and CNC(1000)) are shown in Fig. 1a and b, respectively. Generally, the sizes of the hollow cages prepared at
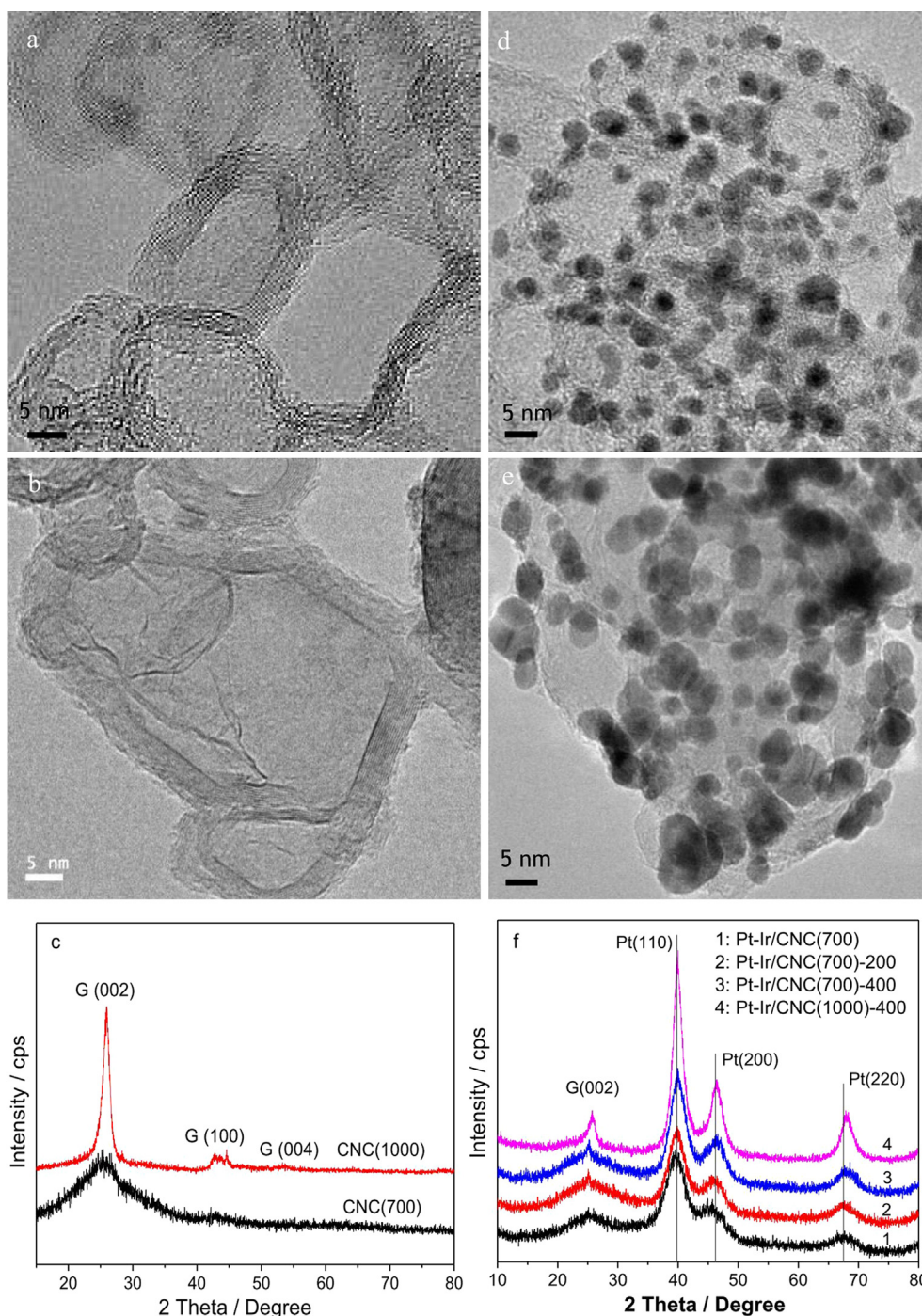

Fig. 1. TEM images of homemade carbon nanocages of CNC(700) (a), CNC(1000) (b) and their XRD patterns (c), and TEM images of Pt−Ir/CNC(700)-400 catalyst (d), Pt−Ir/CNC(1000)-400 catalyst (e) and their XRD patterns (f).

700 °C were 20–50 nm in outer diameter with a shell thickness of ~5 nm, but the sizes for CNCs prepared at 1000 °C were 50–100 nm with a shell thickness of ~10 nm. Obviously, the particle size and the shell thickness increased with increasing preparation temperature. Moreover, the degree of graphitization of CNC(1000) was much higher than that of CNC(700), as shown by their XRD patterns in Fig. 1c. The diffraction peak at $2\theta = 26°$ is ascribed to the diffraction from the 002 planes of graphite. Evidently, this peak for CNC(1000) is stronger and more symmetric than that for CNC(700). For CNCs prepared at 1000 °C, the peaks at $2\theta = 42.6$ and 51° correspond to the (100) and (004) planes of graphite, respectively. The high degree of graphitization of CNC(1000) can also be visualized from the high resolution TEM image displayed in Fig. S1 (Supplementary information-SI). For CNC(700), the graphitic shells were discontinuous with many defects. However, those for CNC(1000) were continuous and thicker, indicating a much higher degree of ordering than CNC(700).

Fig. 1d shows the TEM image of the Pt–Ir/CNC(700)-400 catalyst (heat treated at 400 °C). As can be seen, the dispersion of metal particles was uniform on the carbon support and the shapes of the particles were nearly spherical with a narrow size distribution. The mean particle size of Pt–Ir/CNC(700) catalyst without heat treatment was 2.7 nm (Fig. S2a, SI). After heat treatment at 200 and 400 °C, the metal particle size became 2.9 and 3.5 nm, respectively (Fig. S2b, SI). And the particle size distribution became slightly broader with increasing heat treatment temperature, as revealed by statistical measurements of hundreds of particles (Fig. S2a–e, SI).

Fig. 1e shows the TEM image of the Pt–Ir catalyst supported on CNC(1000) and heat treated at 400 °C (Pt–Ir/CNC(1000)-400). Obviously, when CNCs with a high degree of graphitization were used as the support, the mean particle size of Pt–Ir nanoparticles was the largest among all catalysts (~5 nm). Moreover, the particle size distribution also became much broader, as shown by the result of statistical measurements (Fig. S2f, SI).

Fig. 1f illustrates XRD patterns of different catalysts. As shown, the strong diffraction peaks of all catalysts at $2\theta = 39.5, 46.1$ and 67° are attributed to Pt(111), (200) and (220) crystalline planes, respectively, representing the typical face centered cubic (fcc) crystalline structure of Pt. No characteristic peaks of metallic Ir or Ir oxides were detected. The reason for this observation might be that platinum and iridium had formed solid solutions [26]. For the catalysts using the same support (CNC(700)), the diffraction peaks become sharper and narrower with increasing heat treatment temperature. When CNC(1000) was used as the support, the intensities of the diffraction peaks were the strongest, indicating the largest size and highest degree of crystallinity of Pt–Ir alloy nanoparticles.

Based on Scherrer's formula, the average sizes of metal particles of Pt–Ir/CNC(700), Pt–Ir/CNC(700)-200, Pt–Ir/CNC(700)-400 and Pt–Ir/CNC(1000)-400 catalysts were estimated to be 2.48, 2.86, 3.15 and 4.73 nm, respectively. These sizes are in accord with those results from statistic measurements. In addition, it was found that the peak of the (220) reflection shifted to a higher degree with increasing heat treatment temperature. Especially, for the catalyst supported on CNC(1000), this shift became more identifiable, indicating a lattice contraction arising from the substitution of the smaller Ir atoms for the larger Pt atoms. Such observation suggests that heat treatment gave rise to a high degree of alloying crystallization. The difference in Pt–Ir nanoparticle morphology between different catalysts might be attributed to the difference in the carbon supports used. Namely, the CNCs with a higher degree of graphitization had fewer defective locations for the nucleation of Pt and Ir. Consequently, a larger particle size resulted.

Fig. 2a presents the XPS spectrum of Pt–Ir/CNC(700). The elemental compositions of this catalyst can be calculated and the results are also included. As can be seen, the atomic contents of Pt and Ir in Pt–Ir/CNC(700) were 29.05 and 22.17%, respectively. And, the ICP analysis revealed that the weight percentages of Pt and Ir in
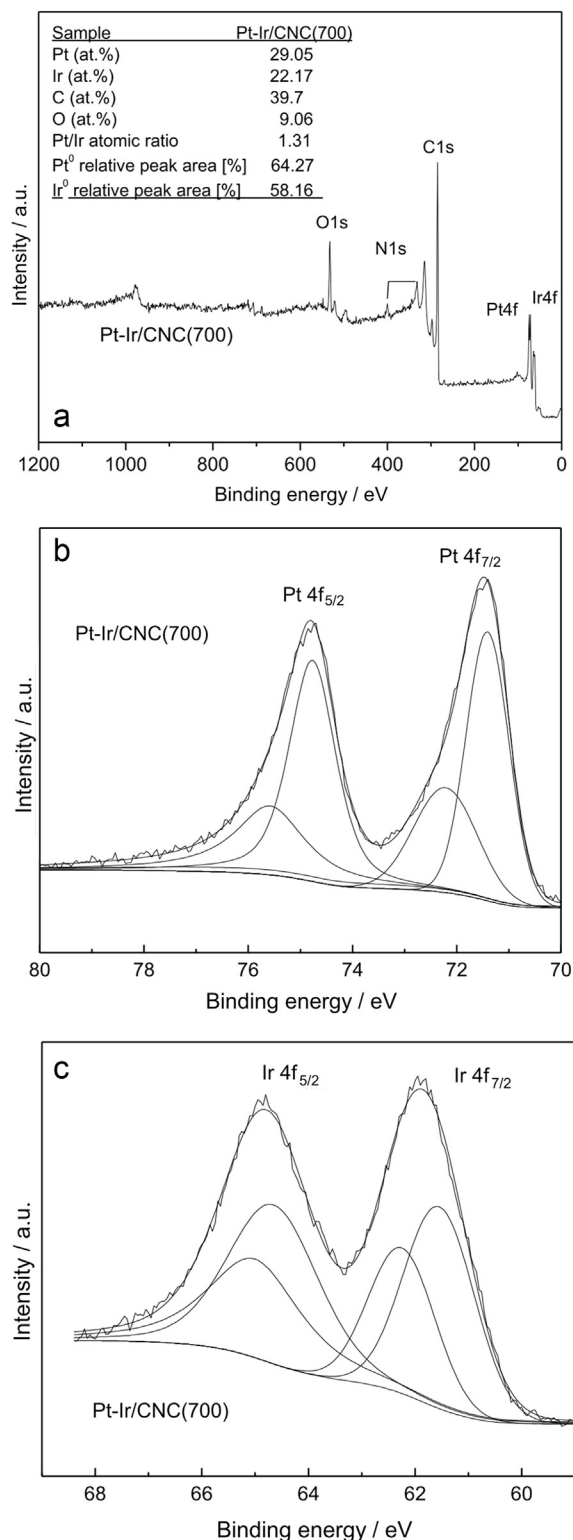

Sample	Pt-Ir/CNC(700)
Pt (at.%)	29.05
Ir (at.%)	22.17
C (at.%)	39.7
O (at.%)	9.06
Pt/Ir atomic ratio	1.31
Pt^0 relative peak area [%]	64.27
Ir^0 relative peak area [%]	58.16

Fig. 2. XPS survey scans and analysis results for Pt–Ir/CNC(700) (a), and XPS core level spectra for Pt 4f (b) and Ir 4f (c) regions of Pt–Ir/CNC(700).

this catalyst were 21.13 and 18.57%, respectively. These results suggest that both Pt and Ir deposited on the carbon support, and their atomic ratio was close to the nominal value of 1:1. Fig. 2b and c shows the XPS spectra of Pt–Ir/CNC(700) for the Pt 4f and Ir 4f regions, respectively. The Pt 4f spectrum has been deconvoluted to two pairs of doublets. The most intense doublet with binding energies of 71.4 eV (Pt 4f$_{7/2}$) and 74.7 eV (Pt 4f$_{5/2}$) is due to metallic Pt. The second doublet pair at 72.2 and 75.5 eV can be attributed to Pt^{2+} as in PtO or Pt(OH)$_2$. The relative intensities of the Pt and Pt^{2+} chemical states are 64.27 and 35.73%, respectively. The Ir 4f spectrum has also been deconvoluted into two different pairs of doublets. 58.16% of the elemental iridium existed as metallic Ir (61.5 and 64.6 eV) and 41.84% occurred as IrO$_2$ (62.2 and 65.0 eV). Thus, it can be seen that elemental platinum and iridium existed mainly as metallic Pt and Ir.

3.2. Electrochemical testing

The electrochemical performance and durability of different catalysts were studied by cyclic voltammetry technique and potential cycling. To remove surface contamination, all electrodes were pre-treated by cycling the potential from 0 to 1.2 V (vs. RHE) at a sweep rate of 100 mV s^{-1} for 50 cycles. To quantify the activity and the difference between different catalysts, the electrochemical active surface area (ECSA) for each catalyst is determined by the following equation:

$$ECSA = Q/(m \cdot \beta) \tag{1}$$

where Q is the charge for hydrogen desorption (mC cm^{-2}), m the quantity of Pt used, and β the charge required to oxidize a monolayer of H$_2$ on bright Pt (=0.21 mC cm^{-2}).

Fig. S3a (SI) displays the initial cyclic voltammograms of Pt–Ir catalysts with different Pt/Ir atomic ratios. Obviously, Pt$_3$–Ir$_1$/CNC(700) demonstrated the strongest hydrogen desorption and adsorption peaks and thus the highest activity than other catalysts. The values of ECSA for Pt$_3$–Ir$_1$/CNC(700), Pt–Ir/CNC(700), and Pt$_1$–Ir$_3$/CNC(700) were calculated to be 57.14, 35.47, and 28.57 m^2 g^{-1}, respectively, suggesting that the catalytic activity decreased with reducing Pt usage. Although the Pt$_3$–Ir$_1$ catalyst showed the best catalytic activity, its usage of Pt was high. Since the catalyst of Pt–Ir/CNC(700) contained a lower percentage of Pt and revealed an ECSA similar to that for the commercial JM catalyst (34.88 m^2 g^{-1}), this catalyst was chosen for further studies.

The durability of Pt–Ir catalysts heat treated at different temperatures were studied by potential cycling and the results are illustrated in Fig. S3b–d (SI). During the accelerated durability test (ADT), the working electrode was a glass carbon electrode with a diameter of 3 mm and the total metal loading was 0.2 mg cm^{-2}. The initial ECSA values for Pt–Ir/CNC(700), Pt–Ir/CNC(700)-200, and Pt–Ir/CNC(700)-400 were 42.5, 35.4, and 44.5 m^2 g^{-1}, respectively. But after 3000 potential cycles, Pt–Ir/CNC(700)-400 showed an obviously higher electrochemical activity than Pt–Ir/CNC(700) and Pt–Ir/CNC(700)-200, with the ECSA being 20.33 m^2 g^{-1} for Pt–Ir/CNC(700)-400 and 12.73 m^2 g^{-1} for Pt–Ir/CNC(700) (Fig. S3d, SI). The ECSA loss for Pt–Ir/CNC(700)-400 after 3000 cycles was 54.33%, whereas that for Pt–Ir/CNC(700) was 70.22%. These results indicate that heat treatment was favorable for the improvement of the catalytic activity and durability of the as prepared Pt–Ir/CNC(700) catalyst.

Pt–Pd alloy catalysts with different atomic ratios supported on CNC(700) were also prepared, and their morphological features were similar to those seen in Fig. 1d for Pt–Ir alloy catalysts. Such catalysts were tested for comparison and the results are presented in Fig. S4 (SI). With increasing the content of Pd, the hydrogen

desorption region changed obviously. That is, the current density increased rapidly with a sharp peak at about 0 V for the catalysts with Pt:Pd ratios of 1:3 and 1:4. This peak was attributed to hydrogen mainly absorbed as β phase, analogous to Pd metal [27,28]. As shown, when the ratio of Pt and Pd was 1:1, the sharp peak disappeared (Fig. S4a, SI). So this catalyst was chosen to be heat treated. After heat treatment, Pt–Pd/CNC(700)-200 (heated at 200 °C) displayed a better activity and durability than Pt–Pd/CNC(700) (unheated) and Pt–Pd/CNC(700)-300 (heated at 300 °C) (Fig. S4b–d, SI).

Now, the Pt–Ir and Pt–Pd catalysts are compared in Fig. 3. The commercial 40 wt.% Pt/C catalyst from Johnson Matthey Co. (JM) was also tested under the same condition for comparison. As shown in Fig. 3a, the initial electrochemical performance was almost the same for JM and Pt–Ir/CNC(700)-400 catalysts, as the values of their ECSAs were 46.4 and 44.5 m^2 g^{-1}, respectively. After ADT, both Pt–Ir/CNC(700)-400 and JM catalysts showed an ECSA decrease with increasing cycling number (Fig. 3b and c). Pt–Ir/CNC(700)-400 held a slow decrease with ~54% loss in ECSA after 3000 cycles. For JM catalyst, however, ECSA decreased rapidly by ~68% from its initial value after 3000 cycles (Fig. 3d). Although Pt–Pd/CNC(700)-200 had a higher ECSA of ~60 m^2 g^{-1} at the initial stage, it degraded rapidly after 1000 potential cycles (Fig. 3b). This catalyst exhibited 82.8% loss in ECSA after 3000 cycles, demonstrating that Ir is advantageous over Pd for alloying with Pt for the improvement of durability. This advantage persists even when the Pt–Ir alloy catalyst is compared with the unalloyed JM catalyst.

Steady-state oxygen reduction reaction (ORR) polarization curves obtained for Pt–Ir/CNC(700)-400 and JM samples in the O$_2$-saturated 0.5 M H$_2$SO$_4$ electrolyte at 1600 rpm are displayed in Fig. 4a. It can be seen that these two catalysts had a similar ORR catalytic activity, ORR onset potential and diffusion-limited current. At higher overpotentials (<0.7 V), the current reached its diffusion-limited value. At lower overpotentials (0.7–0.9 V), the current approached the mixed kinetic/diffusion region. In this region, the half-wave potential of an ORR polarization curve, $E_{1/2}$, is often used to evaluate the electrocatalytic activity of a catalyst. The $E_{1/2}$ values for Pt–Ir/CNC(700)-400 and JM were 0.759 and 0.763 V, respectively. These data reveal that the Pt–Ir/CNC(700)-400 catalyst possessed a similar ORR activity with that for the pure Pt catalyst, although the dosage of Pt was reduced by 50%.

For a better understanding of the observed catalytic activity of the Pt–Ir/CNC(700)-400 catalyst for ORR, the rotating disk electrode (RDE) technique was applied. The kinetic current (i_k) can generally be calculated using the Koutecky–Levich (K–L) equation [29]:

$$\frac{1}{i} = \frac{1}{i_d} + \frac{1}{i_k} \tag{2}$$

where i is the measured current and i_d the diffusion limited current. The i_d term can be obtained from the Levich equation:

$$i_d = 0.62nFAD_O^{2/3}\nu^{-1/6}\omega^{1/2}C_O \tag{3}$$

where n is the number of electrons transferred, F the Faraday constant, A the area of the electrode (0.2463 cm^2), C_O the concentration of oxygen dissolved (1.1 × 10^{-6} mol cm^{-3}), D_O the diffusion coefficient of oxygen in the solution (1.4 × 10^{-5} cm^2 s^{-1}), and ν the cinematic viscosity of sulfuric acid (1.0 × 10^{-2} cm^2 s^{-1}).

Fig. 4b and c shows a set of RDE current–potential curves obtained for Pt–Ir/CNC(700)-400 and JM catalysts in the O$_2$-saturated 0.5 M H$_2$SO$_4$ at 25 °C. K–L plots displayed in Fig. 4d and e presents the relationship between i^{-1} and $\omega^{-1/2}$ and can be used to analyze the order of the ORR with respect to oxygen and to determine i_k values based on the intercepts. The number of electrons transferred (n) was calculated to be ~4 at 0.6–0.75 V from the slopes of the K–L
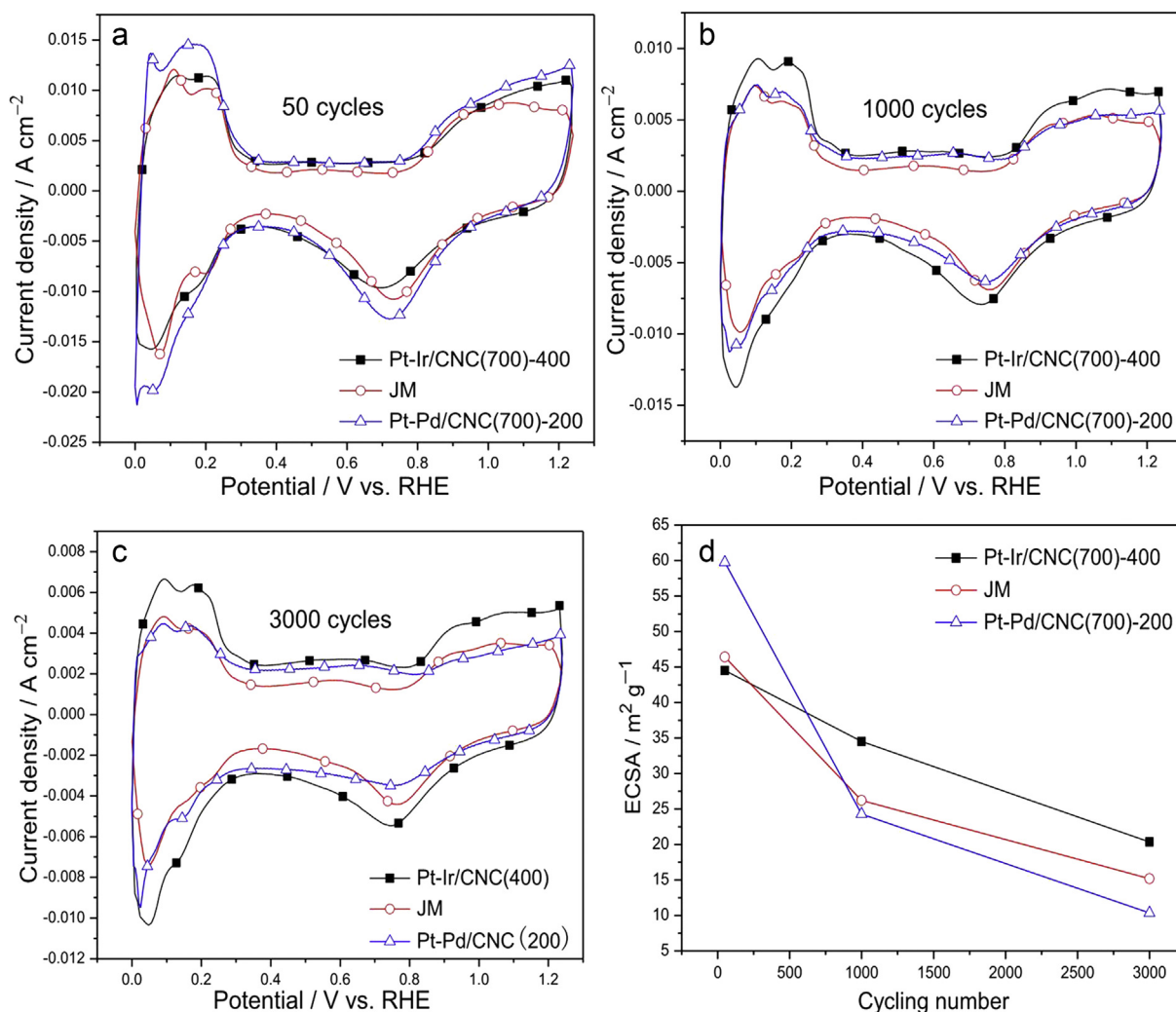
Fig. 3. Cyclic voltammogram curves of Pt–Ir/CNC(700)-400, Pt–Pd/CNC(700)-200 and JM catalysts after different numbers of potential cycling between 0 and 1.2 V (vs. RHE) (a: 50, b: 1000, and c: 3000 cycles) and ECSA comparison among these three catalysts (d). All tests were conducted by using a glass carbon electrode with a diameter of 3 mm as the working electrode and a metal loading of 0.2 mg cm^{-2}.

plots, indicating the nearly complete reduction of O_2 to H_2O on the surface of the Pt–Ir/CNC(700)-400 nanoparticles. i_k values provided a good indication of the ORR kinetics on the surface of a catalyst, while eliminating the effects of reactant diffusion inside the electrochemical cell. The complete reduction of O_2 to H_2O is favorable for stability enhancement of the electrode assembly as incomplete O_2 reduction to H_2O on Pt produces H_2O_2, which creates free radicals that attack the membrane ionomer. The specific activities for Pt–Ir/CNC(700)-400 and JM catalysts at 0.6, 0.65, 0.7, and 0.75 V are presented in Fig. 4f. As shown, the specific activities of Pt–Ir/CNC(700)-400 are much higher than those for JM catalyst.

In order to study the effect of the support material on the durability of the catalyst, the Pt and Pt–Ir alloy catalyst were also supported on the CNCs prepared at 1000 °C (CNC(1000)). During the durability test, the working electrode was an RDE with a diameter of 5.6 mm and the total metal loading was 32.48 μg cm^{-2}. And the durability test was conducted by potential cycling between +0.6 and +1.2 V (vs. RHE) for 3000 cycles in an N_2-saturated 0.5 M H_2SO_4 solution at a scan rate of 100 mV s^{-1}. The cyclic voltammograms of Pt–Ir/CNC(700)-400, Pt–Ir/CNC(1000)-400, Pt/CNC(1000), Pt/CNC(1000)-400 and JM catalysts obtained after 10, 1000 and 3000 cycles are shown in Fig. 5a–e and their ECSA variations with potential cycling number are shown in Fig. 5f. The ECSA

of Pt–Ir/CNC(700)-400 decreased from 48.11 to 9.07 m^2 g^{-1} after 1000 cycles and there was almost no activity after 3000 cycles (Fig. 5a). However, the ECSA for Pt–Ir/CNC(1000)-400 declined from 44.86 to 34.48 m^2 g^{-1} after 1000 cycles and still maintained a value of 18.91 m^2 g^{-1} after 3000 cycles (Fig. 5b). The difference between these two catalysts was the degree of graphitization of the support. CNC(1000) had a higher degree of graphitization than CNC(700), as shown in Fig. 1 and Fig. S1 (SI). This phenomenon demonstrates that a higher degree of graphitization is advantageous for the improvement of durability.

For the unalloyed catalyst using the same support, Pt/CNC(1000), the ECSA also decreased rapidly, from 56.76 to 16.74 m^2 g^{-1} after 1000 cycles, and there was almost no activity after 3000 cycles (only 3.17 m^2 g^{-1} left) (Fig. 5c). The initial electrochemical activity of Pt/CNC(1000)-400 (heated at 400 °C) was much lower than that for Pt/CNC(1000), indicating that heat treatment was unfavorable for pure Pt catalyst. In addition, the durability of Pt/CNC(1000)-400 was also worse than Pt–Ir/CNC(1000)-400. The ECSA of Pt/CNC(1000)-400 decreased from 37.40 to 10.15 m^2 g^{-1} after 1000 cycles, and to only 1.39 m^2 g^{-1} after 3000 cycles (Fig. 5d and f). This result suggests again that Ir alloying with Pt is beneficial for the improvement of stability. For the JM catalyst which was also unalloyed, the ECSA also declined rapidly (Fig. 5e), indicating that an inferior durability
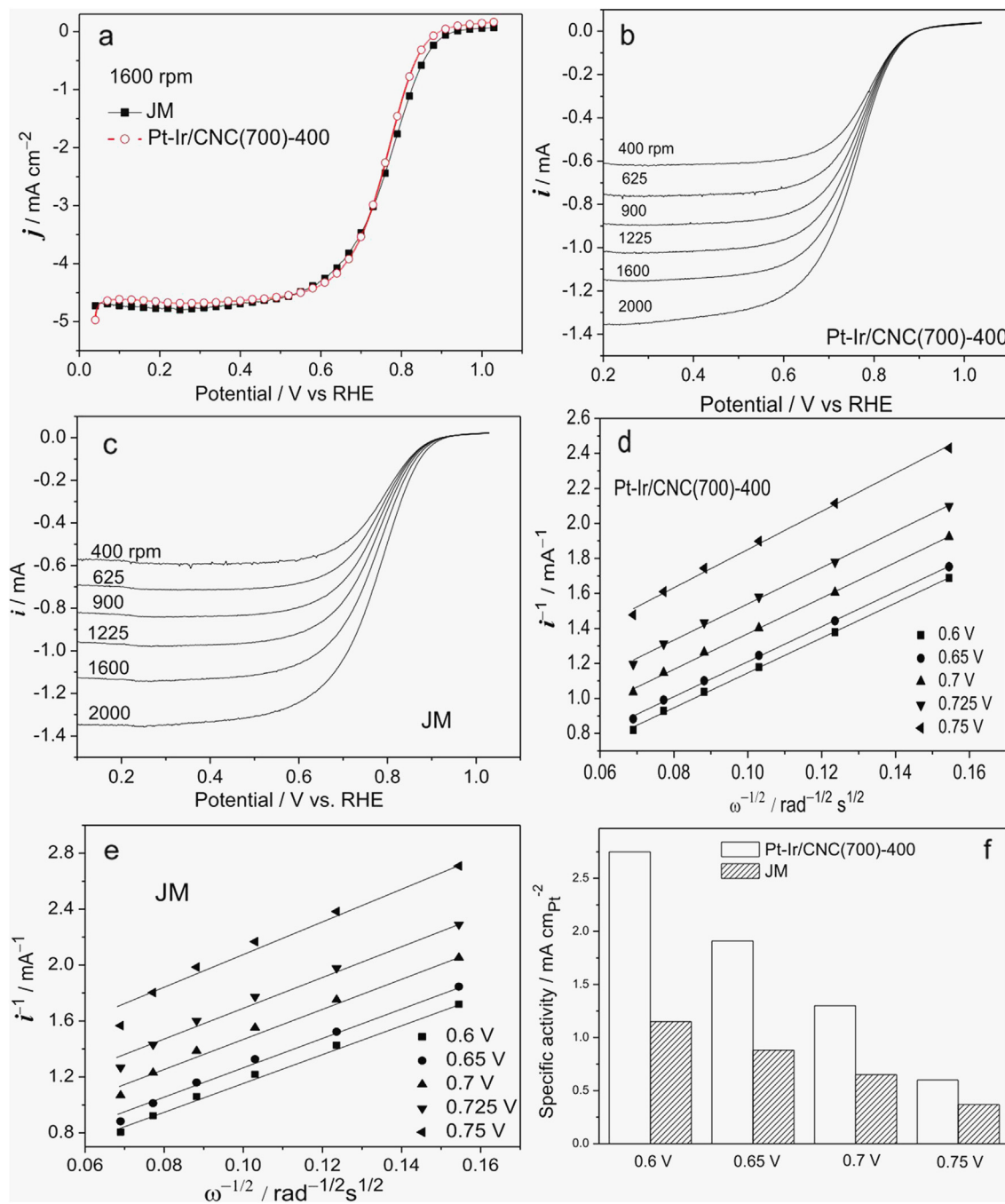
Fig. 4. ORR polarization curves for Pt−Ir/CNC(700)-400 and JM catalysts (a), a set of the rotation-rate-dependent current−potential curves for Pt−Ir/CNC(700)-400 (b) and JM catalyst (c), the Koutecky−Levich plots from (b) and (c) at various potentials (d, e), and comparison of specific activity between Pt−Ir/CNC(700)-400 and JM catalysts (f).

compared with the present Pt−Ir alloy catalyst supported on a graphitic support. The morphologies of Pt and Pt−Ir alloy catalysts, both of which were supported on CNCs, after several thousands of cycling, were examined. Both catalysts showed similar small changes in morphology. The main changes were a small increase of particle size from 3 to 6 nm and a slightly wider distribution from 1.5 to 5 to 3−8 nm, resulting from dissolution and redeposition (Fig. S5, SI). Such changes may be responsible for the observed degradation of catalytic activity.

The ORR polarization curves of Pt−Ir/CNC(700)-400, Pt−Ir/CNC(1000)-400, Pt/CNC(1000) and JM catalysts were also recorded after 10, 1000, 3000 cycles and shown in Fig. 6. As shown in Fig. 6a,

Pt−Ir/CNC(700)-400 exhibited a degradation of 84 mV in half-wave potential $E_{1/2}$ after 1000 potential cycles and even more deterioration of about 246 mV for the next 2000 cycles. However, the degradation of Pt−Ir/CNC(1000)-400 was much slower, with only 49 mV negative shift in $E_{1/2}$ after 1000 cycles and 82 mV for the next 2000 cycles (Fig. 6b). This phenomenon manifests that the use of CNC(1000) with a higher degree of graphitization was also beneficial for the improvement of ORR durability. The advantage of Ir alloying was confirmed by comparing the Pt−Ir alloy catalyst with the Pt catalyst supported on the same CNC(1000) support (Fig. 6c). As shown, the degradation of Pt/CNC(1000) was much larger, with 90 mV negative shift in $E_{1/2}$ after 1000 cycles and
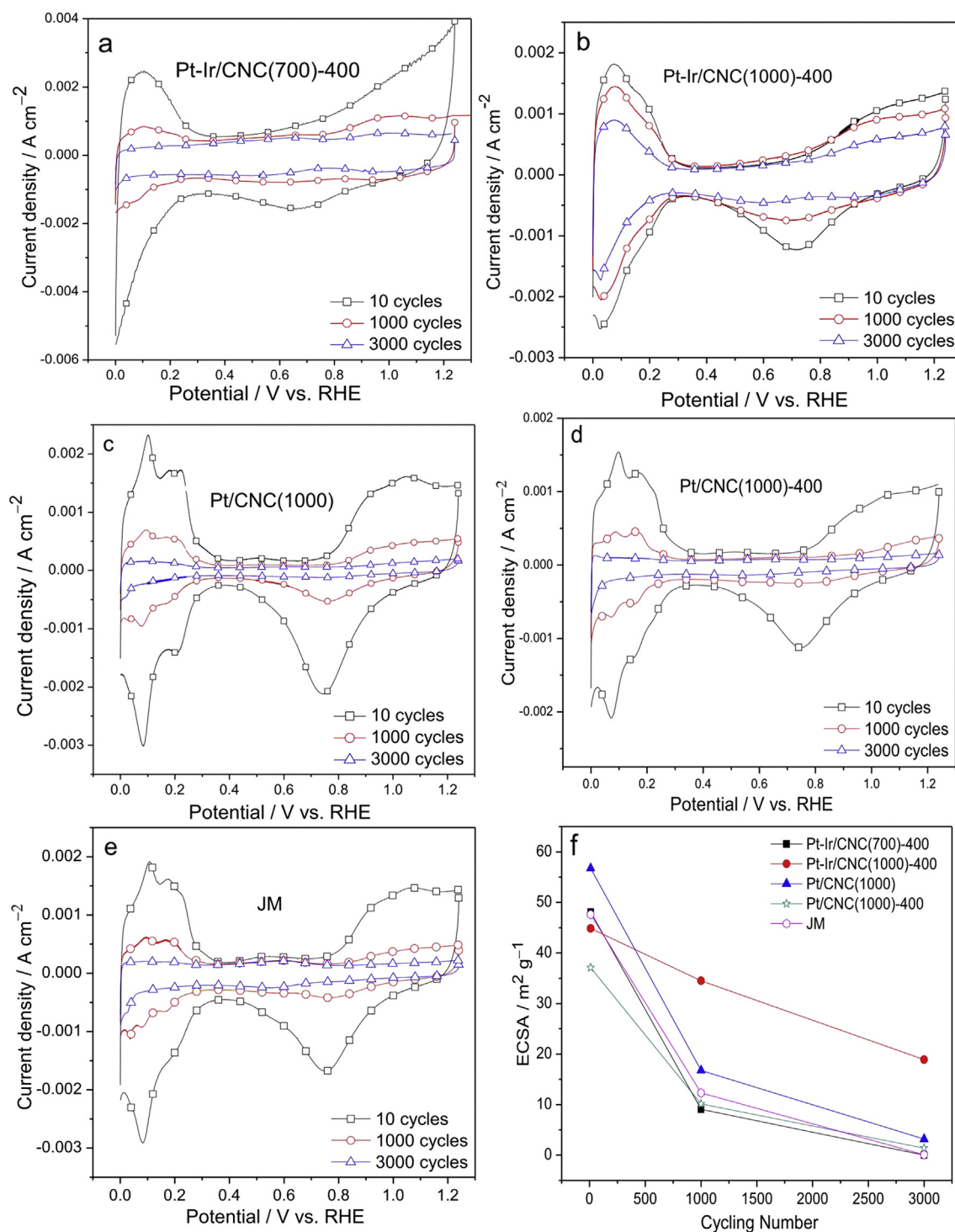
Fig. 5. Cyclic voltammogram curves of Pt–Ir/CNC(700)-400 (a), Pt–Ir/CNC(1000)-400 (b), Pt/CNC(1000) (c), Pt/CNC(1000)-400 (d), JM (e) catalysts after 10, 1000, 3000 potential cycles between 0.6 and 1.2 V (vs. RHE) and the ECSA variation with the cycling number (f). All tests were performed by using a rotating disk electrode with a diameter of 5.6 mm as the working electrode and a metal loading of 32.48 μg cm^{-2}.

104 mV for the next 2000 cycles. The commercial JM catalyst exhibited a similar degradation (Fig. 6d). These experiments were repeated a few times and consistent results were observed, indicating that the Pt–Ir alloy was much more durable and stable than pure Pt for both hydrogen oxidation reaction (HOR) and ORR.

All the above results suggest that the Pt–Ir/CNC(1000)-400 catalyst had a remarkable stability and durability than other catalysts. The main reasons for this could be discussed in two aspects.

Firstly, the support material used in the alloy catalyst was carbon nanocages with a novel structure: hollow interior and graphitic shell. The high degree of graphitization and abundant pores might improve the electrical conductivity of support and facilitate the diffusion of the gas to form a three phase boundary in the catalyst layer. Especially, with increasing the degree of graphitization, the durability was improved significantly. This apparently benefitted from the high corrosion resistance of the graphitic CNCs under
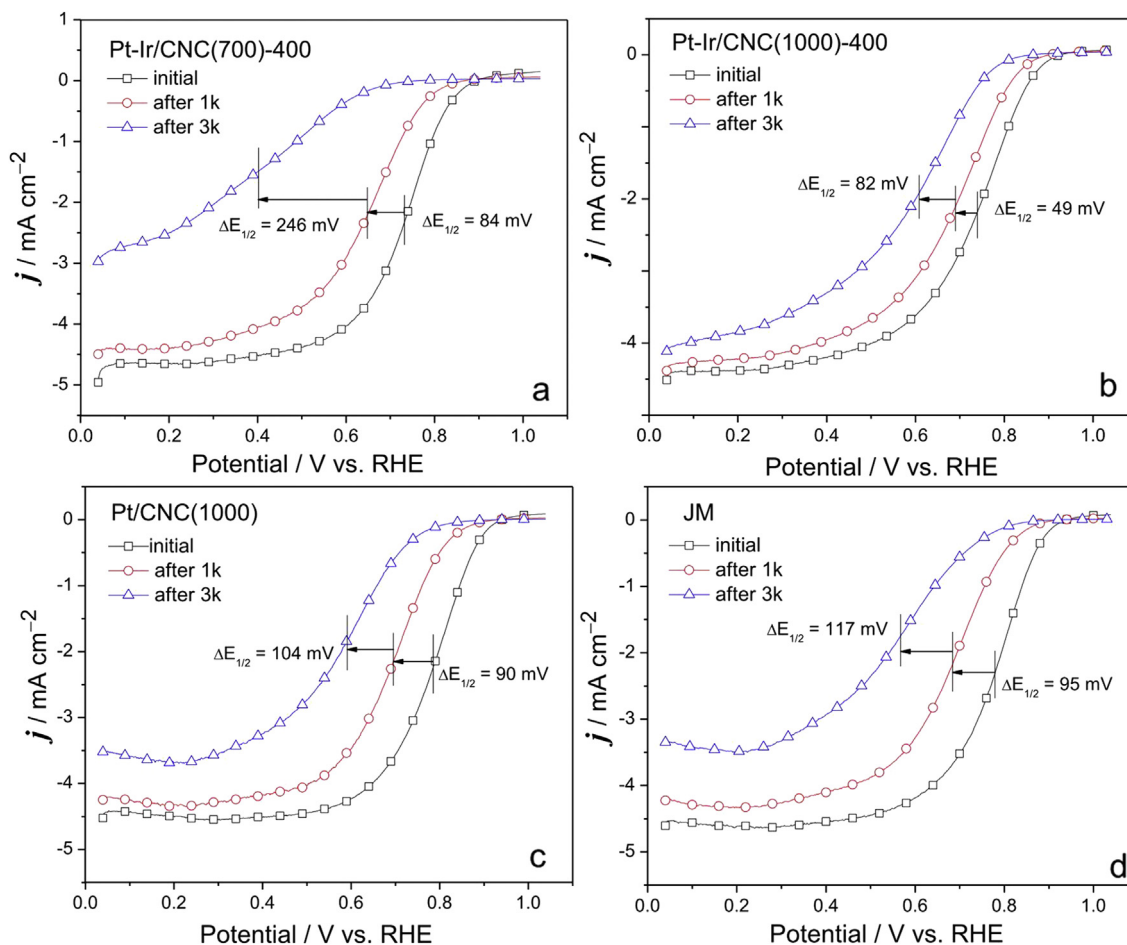
Fig. 6. ORR polarization curves of Pt–Ir/CNC(700)-400 (a), Pt–Ir/CNC(1000)-400 (b), Pt/CNC(1000) (c), JM (d) catalysts after 10, 1000, 3000 potential cycles between 0.6 and 1.2 V (vs. RHE).

electrochemical conditions. Secondly, the use of base metal Ir for alloying is of prime importance. Iridium is a transition metal possessing an excellent stability in acidic media in comparison with other transition metals frequently used for alloying. Such a chemical property could have the advantage in decreasing the dissolution of alloy and favor the stabilization of the alloy catalyst. This suggestion is evidenced by the present sample of Pt–Pd/CNC(700)-200 catalyst showing a lower durability than Pt–Ir alloy and JM catalysts (Fig. 3d). Furthermore, the alloying of Pt–Ir after heat treatment may have changed the nanostructure of the alloy particles with Pt atom congregation on the outmost layers and the Pt–Pt bond distance shortened, introducing surface strain and strong effect on reactivity [30].

At last, the alloying effect may also include the modification of the electronic structure of the catalyst surface [31–35]. Electrons in the inner core orbitals such as Pt 4f or Ir 4f are not directly related to the chemical bonds. However, a change of electron charge density in the valence level orbitals such as Pt 5d or Ir 5d changes potentials inside the atom, so that the binding energy (BE) shift occurs in the core-level electrons [20,26]. As can be seen in Fig. 7, the BE of Pt $4f_{7/2}$ of the catalyst after heat treatment shifted to the positive direction compared with that without heat treatment and pure Pt catalyst, whereas the BE of Ir $4f_{7/2}$ shifted to the negative direction obviously by about 1 eV after heat treatment at 400 °C. These results indicate an intra-atomic charge transfer from the Pt atom to the Ir atom (increase of Pt 5d vacancy). The similar positive BE shift of Pt 4d and Pt 4f spectra for Pt–Ni, Pt–Co, and Pt–Fe alloys was

also observed in a previous study [36]. It was concluded that the positive shift was due to the increased 5d vacancy of Pt, which led to increased π electron donation from O_2 to the surface of Pt, resulting in an increased O_2 adsorption and a weakening of the O–O bond [36,37]. As a result, Pt–Ir/CNC(1000)-400 expressed the best durability both in HOR and ORR.

4. Conclusions

Pt–Ir alloy catalysts supported on CNCs with a Pt:Ir atomic ratio of 1:1 were prepared by EG reduction of Pt and Ir precursors and then heat treatment. Pt–Ir/CNC(700)-400 showed an excellent initial electrocatalytic activity as the commercial JM catalyst. When CNCs with a high degree of graphitization were used as the support, the alloy catalyst had a superior durability and stability over pure Pt catalysts. The graphitic structure of the support and selection of Ir as the alloying element are critical for the improvement of durability. The further reason for the improvement may be the alloying function of Pt and Ir, which modifies the electronic structure and Pt–Pt bond distance of Pt. Considering the observed large difference in electrochemical activity between the present catalyst of Pt–Ir/CNC(1000)-400 and the commercial JM catalyst, alloying with Ir and using the CNCs with a higher degree of graphitization as the support material represent an apparent advance in improving the durability of the Pt catalyst currently in wide use. This study thus provides a new Pt-alloy catalyst for PEMFC with a remarkable durability as well as reduction of the use of Pt by 50 wt.%.
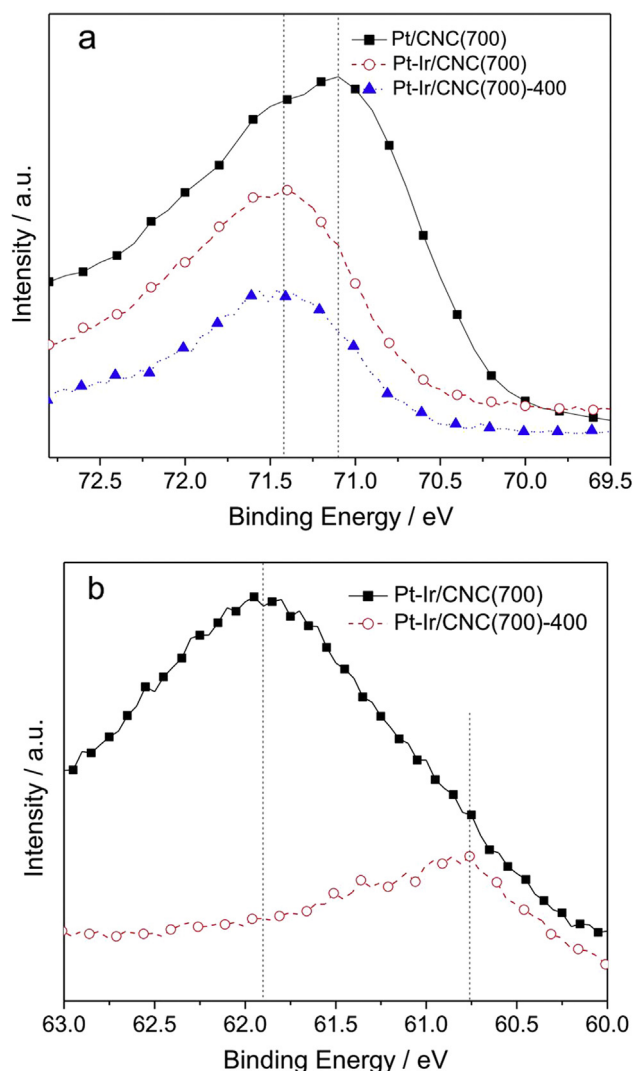
Fig. 7. Core-level XPS spectra of Pt 4f$_{7/2}$ and Ir 4f$_{7/2}$ for Pt/CNC(700), Pt–Ir/CNC(700), and Pt–Ir/CNC(700)-400 catalysts.

Acknowledgments

Appendix A. Supplementary data

Supplementary data related to this article can be found at http://dx.doi.org/10.1016/j.jpowsour.2014.04.097.

References

[1] M.K. Debe, Nature 468 (2012) 43–51.
[2] R. Borup, J. Meyers, B. Pivovar, Y.S. Kim, R. Mukundan, N. Garland, D. Myers, M. Wilson, F. Garzon, D. Wood, P. Zelenay, K. More, K. Stroh, T. Zawodzinski, J. Boncella, J.E. McGrath, M. Inaba, K. Miyatake, M. Hori, K. Ota, Z. Ogumi, S. Miyata, A. Nishikata, Z. Siroma, Y. Uchimoto, K. Yasuda, K. Kimijima, N. Iwashita, Chem. Rev. 107 (2007) 3904–3951.
[3] Y. Shao-Horn, W. Sheng, S. Chen, P. Ferreira, E. Holby, D. Morgan, Top. Catal. 46 (2007) 285–305.
[4] R.M. Darling, J.P. Meyers, J. Electrochem. Soc. 152 (2005) A242–A247.
[5] F. Kadirgan, A.M. Kannan, T. Atilan, S. Beyhan, S.S. Ozenler, S. Suzer, A. Yörür, Int. J. Hydrogen Energy 34 (2009) 9450–9460.
[6] H. Tang, Z. Qi, M. Ramani, J.F. Elter, J. Power Sources 158 (2006) 1306–1312.
[7] E. Antolini, J.R.C. Salgado, E.R. Gonzalez, J. Power Sources 160 (2006) 957–968.
[8] D.L. Wang, H.L. Xin, R. Hovden, H. Wang, Y.C. Yu, D.A. Muller, F.J. DiSalvo, H.D. Abruña, Nat. Mater. 12 (2013) 81–87.
[9] B. Li, J.L. Qiao, D.J. Yang, R. Lin, H. Lv, H.J. Wang, J. Ma, Int. J. Hydrogen Energy 35 (2010) 5528–5538.
[10] Y. Bing, H. Liu, L. Zhang, D. Ghosh, J. Zhang, Chem. Soc. Rev. 39 (2010) 2184–2202.
[11] B.C. Beard, P.N. Ross, J. Electrochem. Soc. 137 (1990) 3368–3374.
[12] L. Xiong, A. Manthiram, J. Electrochem. Soc. 152 (2005) A697–A730.
[13] P.B. Balbuena, D. Altomare, N. Vadlamani, S. Bingi, L.A. Agapito, J.M. Seminario, J. Phys. Chem. A 108 (2004) 6378–6384.
[14] H. Yano, M. Kataoka, H. Yamashita, H. Uchida, M. Watanabe, Langmuir 23 (2007) 6438–6445.
[15] H.R. Colón-Mercado, H. Kim, B.N. Popov, Electrochem. Commun. 6 (2004) 795–799.
[16] H.R. Colón-Mercado, B.N. Popov, J. Power Sources 155 (2006) 253–263.
[17] X. Li, H.R. Colón-Mercado, G. Wu, J.-W. Lee, B.N. Popov, Electrochem. Solid State Lett. 10 (2007) B201–B205.
[18] Z.M. Zhou, Z.G. Shao, X.P. Qin, X.G. Chen, Z.D. Wei, B.L. Yi, Int. J. Hydrogen Energy 35 (2010) 1719–1726.
[19] M.T. Paffett, J.G. Beery, S. Gottesfeld, J. Electrochem. Soc. 135 (1988) 1431–1436.
[20] S. Mukerjee, S. Srinivasan, M.P. Soriaga, J. McBreen, J. Electrochem. Soc. 142 (1995) 1409–1422.
[21] J. Luo, P.N. Njoki, Y. Lin, L.Y. Wang, C.J. Zhong, Electrochem. Commun. 8 (2006) 581–587.
[22] D. Rand, R. Woods, J. Electroanal. Chem. Interfacial Electrochem. 55 (1974) 375–381.
[23] A. Chen, D.J. La Russa, B. Miller, Langmuir 20 (2004) 9695–9702.
[24] M.T. Reetz, M. Lopez, W. Grünert, W. Vogel, F. Mahlendorf, J. Phys. Chem. B 107 (2003) 7414–7419.
[25] W. Chen, S. Chen, J. Mater. Chem. 21 (2011) 9169–9178.
[26] T. Ioroi, K. Yasuda, J. Electrochem. Soc. 152 (2005) A1917–A1924.
[27] H. Li, G. Sun, N. Li, S. Sun, D. Su, Q. Xin, J. Phys. Chem. C 111 (2007) 5605–5617.
[28] M. Łukaszewski, K. Kuśmierczyk, J. Kotowski, H. Siwek, A. Czerwiński, J. Solid State Electrochem. 7 (2003) 69–76.
[29] A. Bard, L. Faulkner, in: Y.H. Shao, G.Y. Zhu, X.D. Dong, B.L. Zhang (Eds.), Electrochemical Methods: Principles and Applications, vol. 9, Chemical Industry Press, 2012, pp. 232–240.
[30] G.A. Somorjai, J.Y. Park, Chem. Soc. Rev. 37 (2008) 2155–2162.
[31] J. Zhang, Y. Mo, M. Vukmirovic, R. Klie, K. Sasaki, R. Adzic, J. Phys. Chem. B 108 (2004) 10955–10964.
[32] J. Zhang, M.B. Vukmirovic, K. Sasaki, A.U. Nilekar, M. Mavrikakis, R.R. Adzic, J. Am. Chem. Soc. 127 (2005) 12480–12481.
[33] J. Zhang, M.B. Vukmirovic, Y. Xu, M. Mavrikakis, R.R. Adzic, Angew. Chem. Int. Ed. 44 (2005) 2132–2135.
[34] M. Shao, T. Huang, P. Liu, J. Zhang, K. Sasaki, M. Vukmirovic, R. Adzic, Langmuir 22 (2006) 10409–10415.
[35] M. Shao, P. Liu, J. Zhang, R. Adzic, J. Phys. Chem. B 111 (2007) 6772–6775.
[36] T. Toda, H. Igarashi, H. Uchida, M. Watanabe, J. Electrochem. Soc. 146 (1999) 3750–3756.
[37] V. Stamenkovic, B.S. Mun, K.J. Mayrhofer, P.N. Ross, N.M. Markovic, J. Rossmeisl, J. Greeley, J.K. Nørskov, Angew. Chem. Int. Ed. 45 (2006) 2897–2901.